The Displacive Phase Transition of Vanadium Dioxide and the Effect of Doping with Tungsten

Makondelele Netsianda,[†] Phuti E. Ngoepe,[†] C. Richard A. Catlow,[‡] and Scott M. Woodley*,[‡]

Materials Modelling Centre, University of Limpopo (Turfloop Campus), Private Bag x 1106, Sovenga 0727, South Africa, and Davy Faraday Research Laboratory, Third Floor, Kathleen Lonsdale Building, Gower Street, University College London, London WC1E 6BT, United Kingdom

Received July 16, 2007. Revised Manuscript Received December 6, 2007

Static-lattice calculations have been employed to model the phases of VO_2 and $V_{1-\delta}W_\delta O_2$. Interatomic potentials were empirically fitted to reproduce the low- and high-temperature phases (monoclinic and tetragonal, respectively) of vanadium dioxide as well as the monoclinic phase of tungsten dioxide. For pure VO_2, we located the soft modes of the high-temperature phase, which characterize the initial atomic displacements that lead to the displacive phase transition to the low-temperature phase. The $T = 0$ structure of the saddle point, where only half of the one-dimensional chains have undergone Peierls distortions, and the ionic motion along the lowest-energy path for the phase transition are described. For $V_{1-\delta}W_\delta O_2$, we found that doping significantly stabilizes the high-temperature phase relative to the low-temperature phase, which explains the observed depression in the transition temperature as δ increases. For the high- and low-temperature phases, the local structures about the dopant, which were obtained by employing a Mott−Littleton approach, resembled those of the low- and high-temperature phases, respectively.

Introduction

Vanadium dioxide provides a classic example of a metal/semiconductor transition. With a critical temperature (T_c) of 341 K,[1] which is tunable over a wide range by doping with, for example, tungsten, pure and doped VO_2 is potentially an ideal material for many different applications: thermochromics, temperature-sensing devices, modulators and polarizers of submillimeter-wavelength radiation, optical data storage media, and variable-reflectance mirrors.[2] The transition temperature of VO_2 decreases at a rate of 11 K/atom % of niobium or molybdenum and 26 K/atom % of tungsten.[3] Thus, the transition temperature can be lowered to 0 °C with, for example, 3 atom % of W (i.e., $\delta = 0.03$) in $V_{1-\delta}W_\delta O_2$.[4]

Regarding the application of infrared-active coatings, Guzman[5] reported that the ability to tune T_c by doping makes tungsten-doped vanadium dioxide useful in energy-efficient or smart windows, which find special applications in the architectural, automotive, and aerospace sectors. An energy-saving surface coating composed of a vanadium dioxide sol−gel solution is particularly useful for the coating of large glass or plastic surfaces such as windows, walls, and windscreens, including windshields. It allows sunlight (both visible and infrared) to penetrate through windows and heat the interior at lower temperatures. When the temperature rises, it switches (as a result of the phase change) to block infrared light from entering the interior while continuing to allow visible light to pass through, thereby reducing the heating of the interior.

In this paper, we report the results of using computer-modeling methods[6] to investigate the displacive phase transition of VO_2 and the effect of doping of W for V.

Structural Properties

The high-temperature tetragonal unit cell, shown in Figure 1a,b, contains two formula units of VO_2 ($Z = 2$) and is more commonly known as the rutile structure, where atoms are located in the general positions of the space group $P4_2/mnm$: $a = b$, 4(e) $\pm (x, y, z; x, {}^1/_2 - y, z + {}^1/_2)$.[7–9] For convenience, as we will be comparing the structures of the two phases, we now redefine the axes as shown in Figure 1a,b so that $b = c$. The rutile structure can be viewed as corner-sharing VO_6 octahedra, except along the a axis, where the octahedra are edge-sharing. The VO_6 octahedra are Jahn–Teller dis-

* To whom correspondence should be addressed via e-mail: Scott.Woodley@ucl.ac.uk.
[†] University of Limpopo.
[‡] University College London.

(1) Rakotoniaina, J. C.; Mokranitamellin, R.; Gavarri, J. R.; Vacquier, G.; Casalot, A.; Calvarin, G. *J. Solid State Chem.* **1993**, *103*, 81–94.
(2) Dachuan, Y.; Niankan, X.; Jingyu, Z.; Xiulin, Z. *J. Phys. D: Appl. Phys.* **1996**, *29*, 1051–1057.
(3) Tang, C.; Georgopoulos, P.; Fine, M. E.; Cohen, J. B.; Nygren, M.; Knapp, G. S.; Aldred, A. *Phys. Rev. B* **1985**, *31*, 1000–1011.
(4) Sella, C.; Maaza, M.; Nemraoui, O.; Lafait, J.; Renard, N.; Sampeur, Y. *Surf. Coat. Technol.* **1998**, *98*, 1477–1482.
(5) Guzman, G. Vanadium dioxide as infrared active coating, 2000. The Sol−Gel Gateway Web site. http://www.solgel.com/articles/August00/thermo/Guzman.htm (accessed Dec 31, 2007).
(6) Catlow, C. R. A. In *New Trends in Materials Chemistry*; Catlow, C. R. A., Cheetham, A., Eds.; NATO Science Series C, Vol. 498; Kluwer Academic: Dordrecht, The Netherlands, 1997.
(7) McWhan, D. B.; Marezio, M.; Remeika, J. P.; Dernier, P. D. *Phys. Rev. B* **1974**, *10*, 490–495.
(8) Wentzcovitch, R. M.; Schulz, W. W.; Allen, P. B. *Phys. Rev. Lett.* **1994**, *72*, 3389–3392.
(9) Kurmaev, E. Z.; Cherkashenko, V. M.; Yarmoshenko, Y. M.; Bartkowski, S.; Postnikov, A. V.; Neumann, M.; Duda, L. C.; Guo, J. H.; Nordgren, J.; Perelyaev, V. A.; Reichelt, W. *J. Phys.: Condens. Matter* **1998**, *10*, 4081–4091.

10.1021/cm701861z CCC: $40.75
Published on Web 02/15/2008

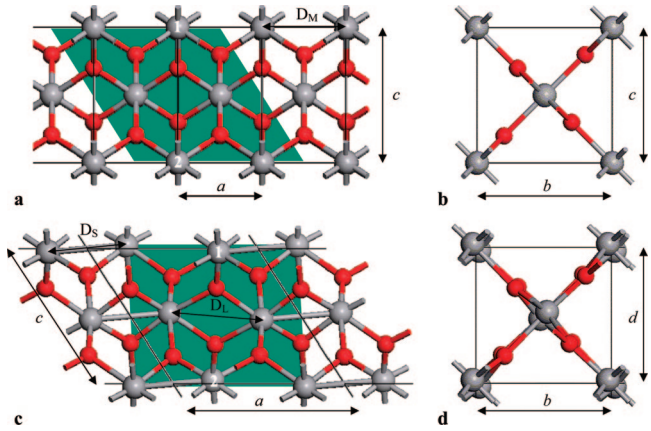

Figure 1. Ball-and-stick representation, as seen from two perpendicular views, of the (a, b) tetragonal (high-temperature) and (c, d) monoclinic (low-temperature) phases of VO_2. Small red and large gray balls represent the oxygen and vanadium atoms, respectively. The short, medium, and long V−V distances (of lengths D_S, D_M, and D_L, respectively) are labeled, and D_S is also indicated via the use of a gray stick. We have labeled the shortest side of the rutile unit cell as *a* rather than *c*, so that its direction is equivalent to the *a* direction in the monoclinic phase. The green-shaded regions indicate two alternative unit cells.

torted from a symmetric octahedral geometry such that four of the six V−O bonds are shorter; from the central vanadium ion, the longer bonds point to the two corner-shared oxygen anions, each of which is part of two edge-sharing octahedra (oxygen anions are threefold-coordinated). Another study[10] found the reverse distortion, in which the four V−O bonds that connect neighboring vanadium ions through edge-sharing faces are longer rather than shorter, yielding the favorable consequence of an increased separation between the highly charged cations. Unless we explicitly state otherwise, we will follow ref 7 when referring to observed data, since the Jahn–Teller distortion is similar to that seen in the low-temperature phase (as discussed in the Results and Discussion).

The low-temperature monoclinic unit cell contains four formula units of VO_2 ($Z = 4$) and is described by the lower-symmetry space group $P2_1/c$ (C_{2h}^5). The crystallographic data used in this work are taken from refs 11 and 12. A crucial feature of this structure is the Peierls distortion along the edge-sharing VO_6 chains, which results in the formation of short (D_S) and long (D_L) V−V interatomic distances of 2.6541 and 3.1246 Å, respectively, rather than just one unique medium distance (D_M) of 2.8514 Å as in the high-temperature tetragonal phase. The local environment around each vanadium atom shows V−O bond distances of 1.760−2.050 Å and O−O separations within the VO_6 octahedron of 2.500−2.900 Å.

The relationship between the rutile ($Z = 2$) and monoclinic ($Z = 4$) unit cells of VO_2 is shown in Figure 1. Although the respective unit cells, each marked using a black box, are significantly different, we note that the displacements of the atom positions required for the change from one phase to the other are small and consist mainly of slight distortions of the chains of VO_6 octahedra. For the high-temperature phase, these chains are collinear with the *a* axis, whereas they form a zigzag array in the monoclinic phase. Above the transition temperature, the metallic phase exhibits paramagnetic behavior, while below the transition temperature, the semiconductor phase is diamagnetic as a result of the metal−metal bonding.

Methodology

All of the calculations, including the empirical fitting of the interatomic potentials and the atomistic simulations, were performed using the General Utility Lattice Program (GULP).[13–15] Cations and anions were modeled using the rigid-ion[16] and shell[17] models, respectively. To model the short-range interactions between ions, we employed a potential-energy function commonly used in modeling of inorganic oxides, the Buckingham potential V_M:

$$V_{\text{Buckingham}}(r) = A_{ij}\exp(-r_{ij}/\rho_{ij}) - C_{ij}/r_{ij}^{\,6} \qquad (1)$$

where r_{ij} is the interatomic distance between ions i and j and A_{ij}, ρ_{ij}, and C_{ij} are species-dependent parameters. However, in order to provide a driving force for the Peierls distortion, we included an additional interaction between cations that was described by a Morse potential:

$$V_{\text{Morse}}(r) = D_{ij}\{1 - \exp[-\alpha_{ij}(r_{ij} - r_0)]\}^2 - D_{ij} \qquad (2)$$

where r_{ij} is the distance between cations i and j and D_{ij}, α_{ij}, and r_0 are also species-dependent parameters. We note that this potential is widely used in modeling species with covalent interactions. Lattice energies and derivatives (i.e., forces) were calculated using standard summation procedures, with the Coulomb interactions being treated using the Ewald method.[18]

We used two least-squares fitting procedures: (1) the ions were fixed at the positions reported by experimental data, and the resultant forces on ions were minimized during the fitting procedure; and (2) the ions were allowed to relax to equilibrium, but the differences between the observed and calculated ionic positions were minimized. The second fitting scheme was used to refine the parameter values found using the first approach. During the derivation of our potential parameters, we wished to influence the fitting procedure in order to ensure that the low-temperature phase would be more stable than the high-temperature phase at 0 K. To accomplish this, we included as an observable in both schemes a small positive difference in the internal lattice energies.

Because we were modeling $V_{1-\delta}W_\delta O_2$, it was important to have the same potential parameters for the anion−anion interactions in both the pure vanadium and tungsten dioxide phases. Initially, we included only the structural parameters of the two vanadium dioxide phases.[7,12] During the final fitting procedure, the structural parameters of the monoclinic phase of WO_2 were also included;[12] initial values of the potential parameters for the interaction between tungsten and oxygen ions were set equal to those found for the interaction between vanadium and oxygen ions. The parameters for the Morse interaction between vanadium and tungsten ions, which were required for modeling the doped system, were calculated simply by averaging the Morse parameters obtained for the V−V and W−W interactions.

(10) Rogers, K. D. *Powder Diffr.* **1993**, *8*, 240–244.
(11) Andersson, G. *Acta Chem. Scand.* **1956**, *10*, 623–628.
(12) Wyckoff, R. W. G. *Crystal Structures*, 2nd ed.; Wiley Interscience: New York, 1965; Vol. 1.
(13) Gale, J. D. *Philos. Mag. B* **1996**, *73*, 3–20.
(14) Gale, J. D. *J. Chem. Soc., Faraday Trans.* **1997**, *93*, 629–637.
(15) Gale, J. D.; Rohl, A. L. *Mol. Simul.* **2003**, *29*, 291–341.
(16) Born, M.; Huang, K. *Dynamical Theory of Crystal Lattices*; Oxford University Press: Oxford, U.K., 1954.
(17) Dick, B. G., Jr.; Overhauser, A. W. *Phys. Rev.* **1958**, *112*, 90–103.
(18) Ewald, P. P. *Ann. Phys.* **1921**, *369*, 253–287.

We obtained significantly better results during our fitting procedures when partial rather than formal charges were employed. As the high-temperature phase of VO_2 has structural properties similar to those of rutile TiO_2, we employed partial charges similar to those used in molecular dynamics studies of TiO_2 microclusters (2.196*e* for Ti and −1.098*e* for O),[19] and V and W cores were assigned charges of +2.200*e* . Unlike the studies of TiO_2, which employed the rigid model, the shell model was used in this work to describe the polarizability of the free anion, as noted above. In our fitting procedure, the charge on the anion shell (*Y*) was fixed; thus, we performed several fits in which different values for *Y* were used but the net charge of the anion was always kept at −1.100*e*.

From diagonalization of the dynamical matrix (which is related to the Hessian, or second derivatives of the internal energy), the eigenvalues (which are the squares of the frequencies) and eigenvectors of the vibrational modes of the crystal structure can be calculated.[20] To determine that a relaxed structure was stable, we checked, with various **k**-points in the first Brillouin zone, that no eigenvalue had a negative value (corresponding to an imaginary frequency); throughout this paper we will refer to an imaginary mode as having a negative frequency. Assuming that only one mode is soft and has a minimum at the Γ point (so that use of a supercell is not required), the eigenvector (at Γ) corresponding to any such eigenvalue points in the direction of steepest descent on the energy landscape, i.e., it indicates how to distort the structure away from a saddle point and toward a local minimum. Determining the lowest-energy path in the case where two degenerate soft modes are present requires mapping the local, two-dimensional energy landscape spanned by the two eigenvectors, as discussed in more detail later. We employed the algorithms based on Newton–Raphson techniques that are available within the GULP code[14] in order to locate both local minima and saddle points (stationary points with zero and one negative eigenvalue of the Hessian, respectively). More precisely, to locate a saddle point, we used the rational functional optimization (RFO) technique, in which a search follows the path of the Hessian mode with the smallest eigenvalue. We note, however, that eigenvector following in which a different mode is selected could also be performed, so that the RFO optimizer could locate various possible transition states starting from a given position. A more detailed description of the RFO technique is given in ref 21.

To model the VO_2 phase transition, a supercell for the tetragonal structure had to be constructed. In order for this supercell to contain the same number of constituent ions as found within the unit cell for the monoclinic phase, one could simply choose to double the shortest length and use a 2 × 1 × 1 supercell. However, constraints imposed by periodicity would create an artificially large energy barrier between the two phases. The cations labeled 1 and 2 in Figure 1a are equivalent, whereas the same cations labeled in Figure 1c are different; the monoclinic phase has two different cation sites. If the green quadrilateral in Figure 1c is assumed to be the unit cell, then the image of V1 along the *d* axis would be less than 0.1 Å from V2. A phonon instability at $\mathbf{k} = (^1/_2, 0, ^1/_2)$ was predicted from diffuse X-ray scattering measurements[22] and from band structure calculations[23] on metallic VO_2. This initially suggested the use of a 2 × 1 × 2 supercell (or the equivalent 2 × 2 × 1 supercell), which would place two vanadium ions along the *a* axis (for the Peierls distortion) and remove the previously discussed V1/V2 problem in the *c* (or *b*) direction. However, comparison of the two structures in Figure 1 showed that it was possible to construct the tetragonal structure using the lower-symmetry but equivalent unit cell indicated by the green quadrilateral (each of whose corners is midway between two vanadium ions) in Figure 1a. A direct mapping between the two phases could then be performed. In modeling the phase transition, all calculations on the tetragonal phase were conducted using this $Z = 4$ unit cell. Both lattice energies and free energies of the phase transition were calculated; in the latter case, the vibrational entropy was calculated using the quasi-harmonic approximation, as outlined by Gale.[14]

We wished to model the effect of doping the two phases of vanadium dioxide with tungsten by replacing one vanadium cation with a tungsten cation to create a defect in the limit of infinite dilution. The solution energy of tungsten in both the high- and low-temperature phases of VO_2 may be calculated by adding the substitution energy, or defect energy, to the difference in the total lattice energies of the pure phases:

$$E_{\text{solution}} = E_{\text{substitution}} + [E_{\text{lattice}}(\text{VO}_2) - E_{\text{lattice}}(\text{WO}_2)] \tag{3}$$

The defect energies were calculated using the Mott−Littleton approach, which is described in detail elsewhere.[24,25] In essence, however, this approach divides the crystal into several regions, each defined by two spherical boundaries centered on the defect; we increased these radial cutoffs in order to converge the defect energy. In our case, the innermost region, for which we used a radial cutoff of 15 Å, contained more than 1400 ions.

The calculated solution energies for the two phases provide an estimate of how the transition temperature for VO_2 will change when the system is doped with tungsten. For the phase transition at the critical transition temperature, there is no change in the Gibbs free energy (*G*), so for the pure system we have

$$\Delta G_0 = \Delta H_0 - T_{c,0}\Delta S_0 = 0 \tag{4}$$

where Δ*H* and Δ*S* are the changes in enthalpy (or internal energy) and entropy, respectively, for the phase transition, T_c is the critical transition temperature, and the subscript 0 refers to the pure phase. Therefore, rearranging eq 4 gives the entropy change as

$$\Delta S_0 = \frac{\Delta H_0}{T_{c,0}} \tag{5}$$

Similarly, for the doped system we have

$$\Delta S = \frac{\Delta H}{T_{c,0} + \delta T_c} \tag{6}$$

where δT_c is the change in the transition temperature upon doping ($\delta T_c = T_c - T_{c,0}$).

Because coordination of the ions is equivalent in the pure and doped systems, we can assume that the change in the entropy

(19) Collins, D. R.; Smith, W.; Harrison, N. M.; Forester, T. R. *J. Mater. Chem.* **1996**, *6*, 1385–1390.
(20) See, for example: Dove, M. T. *Introduction to Lattice Dynamics*; Cambridge University Press: Cambridge, U.K., 1993.
(21) Banerjee, A.; Adams, N.; Simons, J.; Shepard, R. *J. Phys. Chem.* **1985**, *89*, 52–57.
(22) Terauchi, H.; Cohen, J. B. *Phys. Rev. B* **1978**, *17*, 2494–2496.
(23) Gupta, M.; Freeman, A. J.; Ellis, D. E. *Phys. Rev. B* **1977**, *16*, 3338–3351.
(24) Mott, N. F.; Littleton, M. J. *Trans. Faraday Soc.* **1938**, *34*, 485.
(25) Lidiard, A. B.; Norgett, M. J. In *Computational Solid State Physics*; Hermann, F., Dalton, N. W., Koehler, T. T., Eds.; Plenum: New York, 1972; pp 385–412.

Table 1. Parameters for the Short-Range Interatomic Potentials[a]

interaction	A (eV)	ρ (Å)	C (eV Å^6)	interaction	D (eV)	α (Å^{-1})	r_0 (Å)
$V^{q+}-O^{s-}$	15585.5	0.1941	27.25	$V^{q+}-V^{q+}$	0.5270	11.720	2.620
$W^{q+}-O^{s-}$	15995.3	0.2030	30.00	$V^{q+}-W^{q+}$	1.0050	11.800	2.430
$O^{s-}-O^{s-}$	23090.8	0.2342	29.80	$W^{q+}-W^{q+}$	0.7660	11.760	2.525

[a] The harmonic spring constant between each oxygen shell (O^{s-})−core (O^{c+}) pair was 9.85 keV Å^{-2}, and the charges were $q = 2.2e$, $c = 0.12e$, and $s = 1.22e$.

Table 2. Relaxed Values of Structural Parameters and Their Percentage Differences from Observed Values

phase	a (Å)	Δa (Å)	b (Å)	Δb (Å)	c (Å)	Δc (Å)	β (deg)	$\Delta\beta$ (deg)	ΔV (Å^3)
α-VO_2[a]	2.8600	0.30	4.5528	−0.04	4.5528	−0.04	90.0000	0.00	0.22
α-VO_2[b]	5.7199	0.30	4.5528	−0.04	5.3766	0.06	122.1359	0.07	0.22
β-VO_2	5.5883	−2.69	4.5835	1.47	5.3698	−0.10	121.4383	−0.96	−0.09
β-WO_2	5.6207	1.00	4.8066	−1.75	5.5573	−1.64	120.4449	−1.84	0.00

[a] Data presented using the standard tetragonal cell. [b] Data presented using the monoclinic supercell (for ease of comparison with the data for the monoclinic phase).

at the transition point is small, which justifies the approximation $\Delta S_0 \approx \Delta S$; using this approximation to combine eqs 5 and 6 yields

$$\delta T_c = T_{c,0}\frac{\Delta H - \Delta H_0}{\Delta H_0} \quad (7)$$

Now we define the difference in the enthalpies of the doped and pure systems as $\delta H = H - H_0$, so for each phase we have

$$H = H_0 + \delta H \quad (8)$$

Substituting eq 8 into eq 7 gives

$$\delta T_c = T_{c,0}\frac{\Delta(\delta H)}{\Delta H_0} \quad (9)$$

From our Mott−Littleton calculations we can obtain the solution energy, which is the energy of substitution of W into the pure VO_2 phase in the limit of infinite dilution.

Assuming the concentration of dopants for a particular phase to be small enough that we can neglect the interactions between W ions gives

$$\delta H = nH_{solution} \quad (10)$$

where n is the fraction of substituted sites. Substituting eq 10 into eq 9, we find that

$$\delta T_c = T_{c,0}\frac{n\Delta H_{solution}}{\Delta H_0} \quad (11)$$

Therefore, the change in the phase transition temperature upon doping is directly proportional to the difference in the solution enthalpies of the two phases and inversely proportional to the difference in the enthalpies (internal enthalpy) of the pure phases. The use of calculated energies rather than enthalpies in eq 11 is not expected to introduce appreciable errors.

Results and Discussion

Interatomic Potential. Our derived interatomic potential parameters are reported in Table 1 (we used a cutoff of 25.0 Å for the short-range potentials). We use the symbols Ξ_H, Ξ_L, and Ξ_W to refer to our sets of simulated structural parameters (comprising the lattice vectors and internal coordinates) for high-temperature rutile α-VO_2 and low-temperature β-VO_2 and β-WO_2, respectively. These parameters were obtained after minimizing the internal energy (via structural relaxation under constant pressure). Given that we employed only one set of potential parameters for all of the structures, which contain open-shell cations, our simulated parameters Ξ_H, Ξ_L, and Ξ_W matched the observed structural parameters remarkably well (within 2.7%, as reported in Table 2). The structural parameters Ξ_H for the more symmetric phase were within 1% of those observed. The monoclinic phase, which has a combination of Jahn–Teller and Peierls distortions, was much harder to model; the largest error, 2.69%, was found for the a lattice parameter for vanadium dioxide.

With regard to the internal coordinates, our average bond lengths agreed well with the observed values. In particular, for the high-temperature phase, we obtained 1.928 Å (simulated) compared to 1.925 Å (observed), whereas for the low-temperature phase of vanadium dioxide, we found 1.922 Å (simulated) compared to 1.931 Å (observed). This agreement was similar to that achieved in a previous study, where average bond lengths for the high- and low-temperature phases were estimated as 1.926 and 1.940 Å, respectively.[26]

For the high-temperature phase, we obtained two V−O bond lengths of 1.919 Å and four of 1.933 Å. Qualitatively, our predicted distortion was the same as that observed by Rogers.[10] Similarly, for the low-temperature phase, we predicted the reverse Jahn–Teller-distorted environment, although in this case the distortion was dominated by the Peierls contribution (the vanadium ion was no longer midway between pairs of oxygen anions). Thus, in the Peierls distortion, the short bond pair from the high-temperature phase was elongated and split, giving lengths of 1.921 and 1.929 Å, while the fourfold degeneracy of the longer bonds was lifted to yield V−O bond lengths of 1.882 and 1.961 Å for one pair and 1.889 and 1.950 Å for the other. Without explicitly including in our model a functional term that could drive a Jahn–Teller distortion, we were unable to reproduce the qualitative feature of four short and two long bonds about each cation (where we averaged over pairs to remove the Peierls distortion).

During the refinement fitting procedure, the smallest change between observed and simulated unit-cell volumes was targeted. For tungsten dioxide, a perfect agreement was

(26) Wilhelmi, K. A.; Waltersson, K.; Kihlborg, L. *Acta Chem. Scand.* **1971**, *25*, 2675.

Table 3. Nearest-Neighbor Cation−Cation Distances for the Two Phases of VO_2 and for Monoclinic WO_2

	observed		simulated	
phase	D_S (Å)	D_L (Å)	D_S (Å)	D_L (Å)
α-VO_2	2.851	2.851	2.860	2.860
β-VO_2	2.654	3.124	2.659	2.931
β-WO_2	2.486	3.089	2.492	3.140

Table 4. Calculated Lattice Energies (eV/Monoclinic Unit Cell)

phase	internal energy	zero-point energy	free energy at 0 K
α-VO_2	−164.07307	0.68338	−163.38969
β-VO_2	−164.16740	0.75099	−163.41641
β-WO_2	−154.83700	0.60110	−154.23590

obtained, whereas for the two phases of vanadium dioxide, some compromise had to be made. We also tried including the angular overlap model[27] in order to model Jahn–Teller effects explicitly. By reproducing the observed distribution of V−O bond distances in both phases (i.e., four long and two short bonds), we obtained better agreement with the observed lattice parameters. At present, however, the angular overlap model is not available within the free-energy or Mott−Littleton modules of any available codes.

Our model for WO_2 was also reasonable (the errors were less than 1.85% for all components of Ξ_W). However, comparing the relaxation of the two monoclinic phases, we note that the VO_2 *a* and *b* lattice parameters shrank and stretched, respectively, whereas they stretched and shrank for WO_2. The difference in the relaxation patterns nevertheless resulted in good agreement with experiment for the unit-cell volume for both materials.

Phase Transition. For our investigation, it was more important to model the Peierls distortion than the Jahn–Teller effect, as it is the former that distinguishes the two phases of vanadium dioxide. The difference, λ, between the long (D_L) and short (D_S) intercationic distances along the chains of VO_6 edge-sharing octahedra provides the best measure of the Peierls distortion:

$$\lambda = D_L - D_S \tag{12}$$

Because the high-temperature phase has no Peierls distortion, λ is zero for that phase, as seen in both the observed and simulated structures. On the basis of the distances reported in Table 3, λ for our simulated low-temperature phase of VO_2 (0.27 Å) was smaller than the observed value (0.47 Å), as a result of the discrepancy between the observed and simulated values of the longer V−V distance D_L. For WO_2, we obtained much better agreement between the simulated and observed λ values (0.65 and 0.60 Å, respectively).

The internal and zero-point free energies for our simulated pure phases are reported in Table 4. A 5 × 5 × 5 Monkhorst−Pack set of grid points[28] across the first Brillouin zone was used when calculating the zero-point energy (to five significant figures). The low-temperature, monoclinic phase of VO_2 was found to be more stable than the tetragonal phase by 0.027 eV/unit cell [2.58 kJ mol^{-1} $(unit\ cell)^{-1}$] at 0 K.

As we will show, examination of our simulated (internal) energy landscape showed that ϵ_h, the height of the energy barrier for the transition from the high- to the low-temperature phase, was very small, and it was therefore difficult to compute the free energy as a function of temperature for the high-temperature phase. At $T = 0$ K, the lowest optical modes indicated both phases are stable, but as the simulated temperature increased, some of the modes for the high-temperature phase softened. In fact, when the shortest lattice parameter (labeled *a* in Figure 1a) was reduced, the rutile-phase optical mode that softened did so near the **k**-point ($^1/_2$, $^1/_2$, 0) [or ($^1/_2$, 0, $^1/_2$), as the *b* and *c* lattice parameters are equivalent by symmetry].

To obtain an estimate of ϵ_h, we computed the internal energy for the set of intermediate structures Ξ_i:

$$\Xi_i = \Xi_H(1 - f_i) + \Xi_L f_i \tag{13}$$

where f_i is a fractional coordinate and *i* labels points along the shortest transition path between the two phases. Thus, we modeled a linear transition whereby the medium intercationic distances (D_M) of the high-temperature phase gradually become the alternating D_S and D_L series of the low-temperature phase, as shown in Figure 2d. The variations of the phonon bands and the internal energy as a function of *f* are shown in Figure 2a−c. We note that we have used different line types to indicate the different motions of the cations [as determined from the eigenvector components for $f_i = 0$ (i.e., the high-temperature phase) in Figure 2a and $f_i = 1$ (i.e., the low-temperature phase) in Figure 2b]: lines colored black, gray, and light gray signify predominant, some, and negligible amounts of cation movement, respectively, and solid lines indicate strong cation motion along the −V−V− chains. The characteristic motion of some modes evolved (as highlighted by a comparison of parts a and b of Figure 2). For example, in the highest-frequency modes (gray in Figure 2a and black in Figure 2b), the cation motion along the cation chains became stronger in the low-temperature-phase limit, as these modes dramatically hardened. After changes of 18 and 22% from the high- and low-temperature phases, respectively, the softening of two of cation vibrational modes was also quite dramatic. For the high-temperature phase, the cation motion was predominately along the cation chains, whereas for the low-temperature phase, the cation motion was predominately normal to the cation chains and the degeneracy of these modes was lifted (at $f = 0.85$). Upon examination of the corresponding eigenvectors for these degenerate modes in the high-temperature phase, which we defined as $\mathbf{e}_1$ and $\mathbf{e}_2$, it is perhaps not surprising that we found the cations to oscillate, forming short and long V−V distances along the −V−V− chains, as observed in the low-temperature phase. As shown in Figure 1c, there are two −V−V− chains in the monoclinic cell, and rather than having short V−V distances to the right of atom 1 and the left of atom 2, we could equally well have drawn the alternating short–long pattern having short V−V distances to the left of atom 1 and the right of atom 2. For convenience, we label these structures Ξ_{L_1} and Ξ_{L_2}. One of the eigenvectors, say $\mathbf{e}_1$, moves the cations of the high-temperature phase out of equilibrium to give one of these short–long patterns, while the other pattern is obtained using $\mathbf{e}_2$.

(27) Woodley, S. M.; Battle, P. D.; Catlow, C. R. A.; Gale, J. D. *J. Phys. Chem. B* **2001**, *105*, 6824–6830.
(28) Monkhorst, H. J.; Pack, J. D. *Phys. Rev. B* **1976**, *13*, 5188–5192.

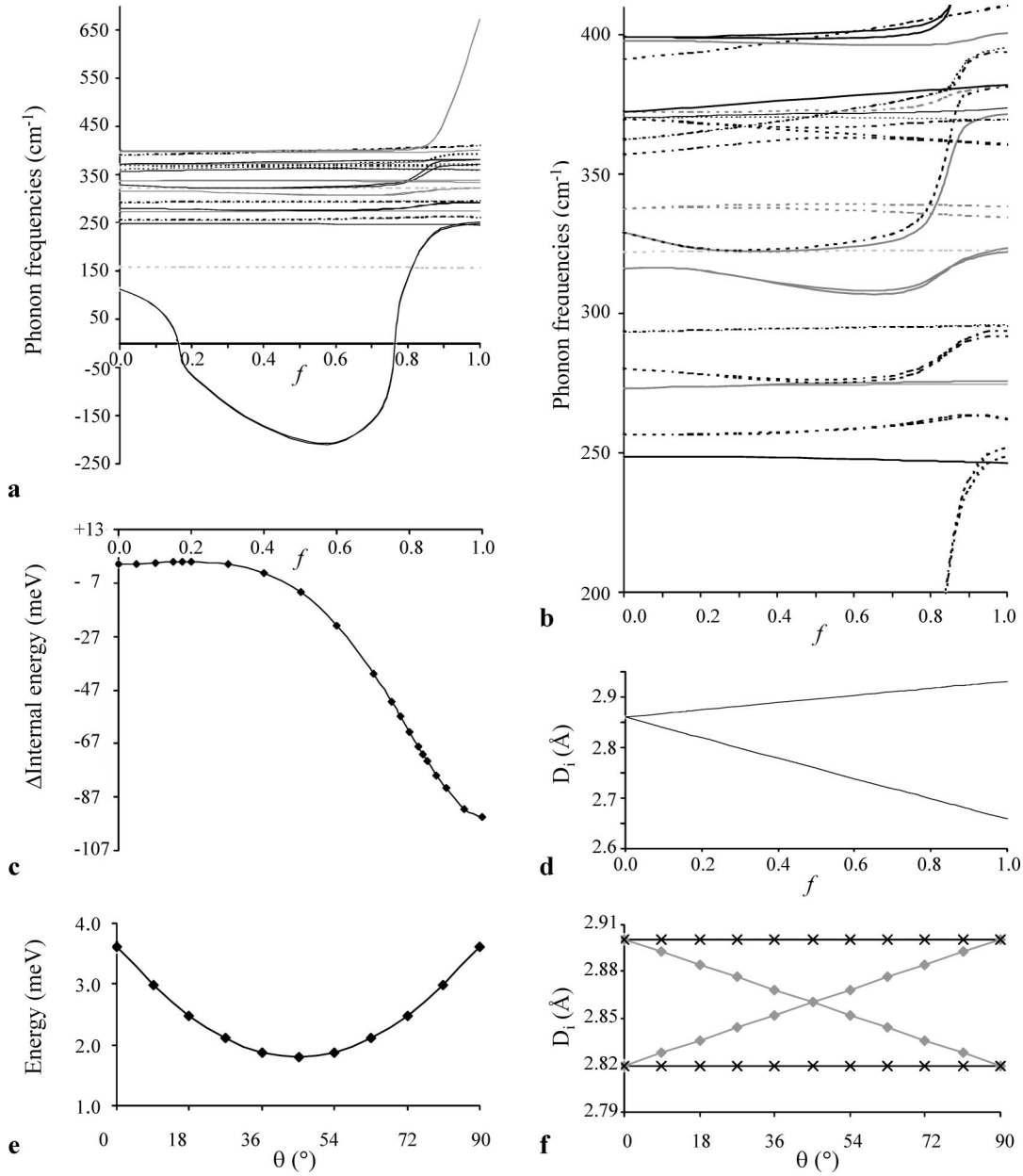

Figure 2. (a, b) Frequency modes at Γ, (c) energies, and (d) V−V distances along a chain at various points on the path f for the linear VO_2 structural phase transition from tetragonal ($f = 0$) to monoclinic ($f = 1$), and (e) energies and (f) V−V distances along a chain for structures along an arc on the energy surface defined by the eigenvectors $\mathbf{e}_1$ and $\mathbf{e}_2$ (see text) of the high-temperature phase.

From Figure 2c, we obtained an estimated value of 0.001 eV/unit cell for ϵ_h. Of course, this is an upper limit for the transition barrier, as a linear transformation may not necessarily be the lowest-energy route. We define Ξ_{hsp} to be the structural parameters of the transition point. In an attempt to locate the saddle point, and therefore the parameters Ξ_{hsp}, we used the RFO optimizer to perform a transition-point search starting from the highest-energy intermediate structure found along the linear transition path (Ξ_i with $f_i \approx 20\%$). Although a saddle point was located, we unfortunately found a structure (defined as Ξ_{lsp}) having an internal energy lower than that of the high-temperature phase. As the high-temperature structure is known to be stable (i.e., at a local minimum), any path from the high- to the low-temperature phase should contain at least one local maximum that is higher than both local minima, and on the path of lowest energy, this maximum is the saddle point that we were trying to locate. Thus, we needed to perform a more careful search of the energy landscape.

Because the modes that soften for the high-temperature phase are degenerate, we needed to determine the initial directions along the lowest-energy path between the two phases. These directions were found by calculating the internal energy along an arc with a fixed radius in the plane spanned by the two degenerate eigenvectors $\mathbf{e}_1$ and $\mathbf{e}_2$, i.e., we calculated the internal energies of the structures Ξ_j given by

$$\Xi_j = \Xi_H + \mu(\mathbf{e}_1 \cos\theta_j + \mathbf{e}_2 \sin\theta_j) \qquad (14)$$

where μ is a small constant and $0 < \theta_j < 90°$ (we note that Ξ_j contains Cartesian rather than fractional coordinates). As Figure 2e shows, the internal energy has a minimum at $\theta_j = 45°$, i.e., one of the initial directions along the lowest-energy path is $^1/_2\mathbf{e}_1 + {}^1/_2\mathbf{e}_2$, while the other is $^1/_2\mathbf{e}_1 - {}^1/_2\mathbf{e}_2$. At $\theta_j =$

Table 5. Saddle- and End-Point Structural Parameters (Ξ_m), Relative Internal Energies per Vanadium Ion ($\Delta E = E - E_L$), and the Four Shortest V−V Distances (D_{V-V}) in VO_2

m	*a* (Å)	*b* (Å)	*c* (Å)	*V* (Å^3)	ΔE (eV)	D_{V-V} in first chain (Å)		D_{V-V} in second chain (Å)	
H	5.7199	4.5528	5.3766	118.565	0.0943	2.860	2.860	2.860	2.860
hsp	5.6993	4.5574	5.3749	118.370	0.0951	2.850	2.850	2.809	2.891
lsp	5.6056	4.5788	5.3675	117.492	0.0543	2.804	2.804	2.661	2.945
L_1 and L_2	5.5883	4.5835	5.3698	117.352	0.0000	2.659	2.931	2.659	2.931

45°, as shown in Figure 2f, there is no Peierls distortion along half of the chains. Moreover, as the system travels along either of the initial lowest-energy paths, only half of the −V−V− chains are distorted. From the local highest-energy structure found along one of these paths, we obtained a better estimate of Ξ_{hsp}. This structure was found to have medium V−V distances along one chain, which were shortened from 2.860 to 2.843 Å, and alternating short and long V−V distances of 2.800 and 2.886 Å, respectively, along the Peierls-distorted chains.

Refining these structural parameters using the RFO approach for locating a transition point, we successfully found the saddle point, with structural parameters Ξ_{hsp}. The V−V distances and lattice constants and the internal energy of the transition point are reported in Table 5, and the structure is shown in Figure 3. The medium V−V distances along one chain were 2.850 Å, whereas the alternating short and long V−V distances along the Peierls-distorted chains were 2.809 and 2.891 Å, respectively. The barrier height, ϵ_h, was 0.001 eV/unit cell (we note that for such systems, one might expect there to be no barrier, but the curvature in the energy landscape of our model was such that there was still significant structural movement). The three lowest-frequency optical modes were –72.31 cm^{-1} (predominantly transverse cation oscillation of the nondistorted chain and longitudinal cation oscillation of the distorted chain), 53.34 cm^{-1} (predominantly longitudinal cation oscillation along the nondistorted chain and transverse cation oscillation of the distorted chain), and 158.86 cm^{-1} (oscillation of anions). Slightly increasing or decreasing the magnitude of the Peierls distortion in the Peierls-distorted chains lowered the internal energy. Thus, interestingly, the non-Peierls-distorted chains break symmetry only after a sufficient distance beyond the saddle point has been reached.

To confirm that we had found the correct saddle point, first we slightly distorted the structure along the direction of the lowest-frequency (imaginary) eigenvector (the anion shells were displaced using the same components as for their respective cores and then optimized, while all other structural parameters were fixed). Then, upon relaxation (using a standard downhill approach with a small step size), we successfully recovered the high-temperature phase. Repeating this procedure, but slightly displacing atoms in the reverse direction, we found the structural parameters Ξ_{hsp} of the lower-energy saddle point, which had lowest-frequency optical modes of –253.1 cm^{-1} (predominantly longitudinal cation oscillation along the nondistorted chain and transverse cation oscillation of the distorted chain) and 157.4 cm^{-1} (oscillation of anions). Repeating the process again, starting from the lower-energy saddle point, we found the two equivalent low-temperature phases Ξ_{L_1} and Ξ_{L_2}. Thus, the original path from the high-temperature structure became a line along a ridge between the regions of the two low-temperature structures, as shown in Figure 4. Further investigation also showed that our first attempt to find the high-energy saddle point using the RFO approach failed because the initial point was already off this symmetry line, and while initially following the lowest eigenvector, the second lowest optical mode simultaneously softened.

To summarize, by searching the energy landscape defined by the two soft modes of the high-temperature phase, we have located the transition point along the lowest-energy transition path from the more symmetrical high-temperature phase to the Peierls-distorted low-temperature monoclinic phase. Before our study, one may have expected that Peierls distortions would occur simultaneously along all one-dimensional (1D) cation chains. However, the structure of the transition point indicated that the initial stabilization caused only half of the 1D cation chains to exhibit the Peierls form of distortion. Such a monoclinic phase, where only half of the 1D chains are distorted, has been observed for $V_{1-\delta}Cr_\delta O_2$, where δ is small but greater than 0.003.[29] Use of a larger supercell, containing more than two 1D chains, may predict that the initial Peierls distortion occurs on an even smaller fraction of 1D chains. After the transition point, the lowest-energy path initially continued along the same direction (increasing Peierls distortions in the Peierls-distorted chains) and then gradually changed direction (the orthogonal direction is the line where the remaining 1D chains are Peierls distorted). We note that if the direction of the path had not changed, then the line of the ridge (indicated by the red line in Figure 4) would have been followed until the path reached the lower-energy saddle point (full Peierls distortion of half of the 1D chains). An investigation of the effect of temperature on this energy landscape will be reported elsewhere.

Dopant Energies. Our calculated energies for substitution of W into the low-temperature monoclinic and high-temperature tetragonal phases were 2.344 and 1.963 eV,

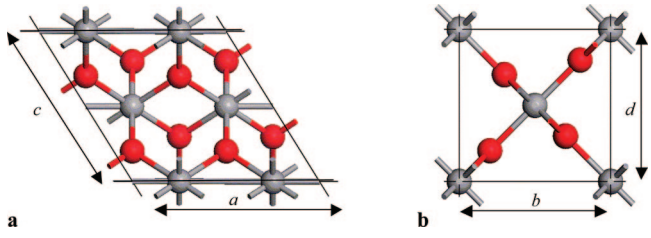

Figure 3. Ball-and-stick model (where sticks indicate V−O bonds and short V−V distances) of the structure of the saddle point for the monoclinic-to-tetragonal phase transition of VO_2.

(29) Pouget, J. P.; Launois, H.; Rice, T. M.; Dernier, P.; Gossard, A.; Villeneuve, G.; Hagenmuller, P. *Phys. Rev. B* **1974**, *10*, 1801–1815.

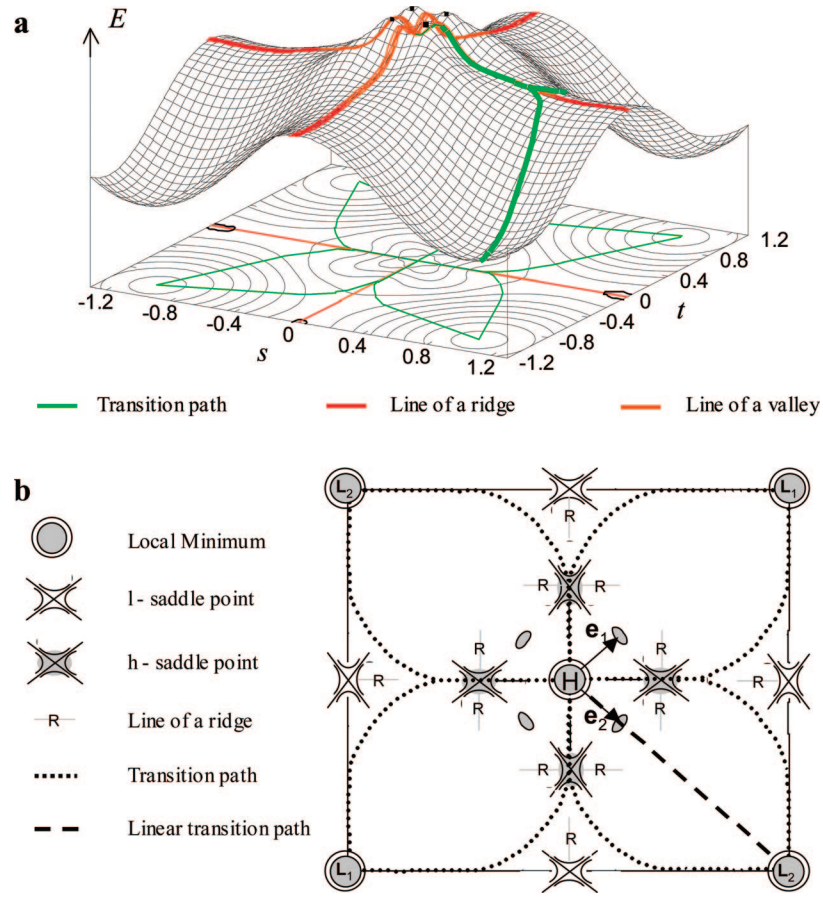

Figure 4. Energy landscape as a function of the two vibrational modes of the high-temperature phase that become soft, viewed as (a) an isosurface with contours drawn below, which is based on (b) the key stationary points of the energy surface. The high-temperature tetragonal phase (H) is found at $s = t = 0.0$, and the low-temperature monoclinic phase (L) is found at $|s| = |t| = 1.0$. Only two of the eight degenerate lowest-energy pathways are shown on the isosurface, and only features discussed in the text are included. The directions of these paths near the global minima were assumed.

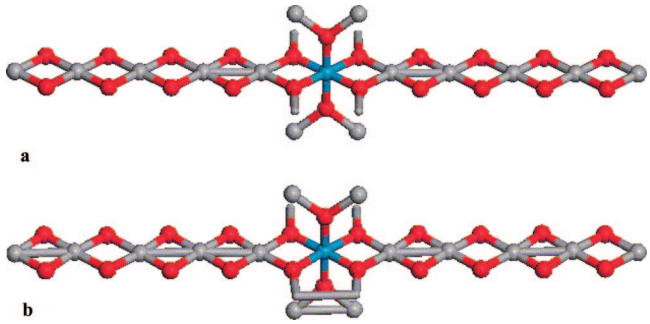

Figure 5. Ball-and-stick model of the defect region of infinitely dilute W-doped (a) tetragonal and (b) monoclinic VO_2 phases.

respectively. Using eq 3, we therefore calculated the solution energies for doping W into the two phases to be –0.011 and –0.3460 eV/dopant atom, respectively. Figure 5 shows the structure of the cation chain containing the W dopant atom, which we call the central chain, as well as a small section of the four parallel, neighboring chains. The changes in the intercationic distances along these chains are reported in Tables 6 and 7. We note that the changes in the V−V distances in going from the tetragonal to the monoclinic phase in pure VO_2 were –0.201 Å (short) or 0.071 Å (long).

For the high-temperature tetragonal phase, we obtained two W−V distances of 2.978 Å within the central chain and four stretched V−V distances (two of 2.901 Å and two of 2.929 Å) in the neighboring chains, which we may compare to the V−V distances of 2.860 Å for the pure phase. To accommodate the larger cation, the two V−V distances in the central chain nearest the W dopant (indicated by the use of a stick in Figure 5a) were shortened to 2.665 Å, and the next-nearest V−V distances in the neighboring chains were shortened by smaller amounts, to 2.842 and 2.818 Å. The next-nearest V−V distances in the central and neighboring chains were closer to those in the pure phase; however, they were longer rather than shorter. Thus, the W cation causes a Peierls distortion that decays with distance from the defect center, and as a result, the doped tetragonal phase contains a small region that resembles the low-temperature monoclinic structure.

In contrast to the pure tetragonal phase, in the monoclinic phase each cation occupies a mirror point of the chain; however, the two W−V distances, of length 2.921 Å, were equivalent. Along one direction of the central chain, we immediately found the pattern of a Peierls distortion: alternating short and long V−V distances. In the other direction, we found two consecutive short V−V distances, which reversed the short–long sequence so that the Peierls distortion was in phase with that of the surrounding lattice. Thus, the W dopant induces two lattice defects: the W site and the site of the consecutive short V−V distances.

Finally, we were able to use eq 11 to calculate a reduction of 48.4 K in the phase transition temperature for a 1%

Table 6. Changes in Intercationic Distances (Å) along the Central (W-Containing) and Four Closest Parallel Chains upon Doping the VO_2 Tetragonal Phase with W[a]

up	0.002	0.003	0.001	−0.042	*0.069*	−0.042	0.001	0.003	0.002			
front	0.002	0.006	−0.011	−0.018	*0.041*	−0.018	−0.011	0.006	0.002			
central	0.002	0.005	0.067	−0.195	**0.118**	**0.118**	−0.195	0.067	0.005	0.002		
down	0.002	0.006	−0.011	−0.018	*0.041*	−0.018	−0.011	0.006	0.002			
back	0.002	0.003	0.001	−0.042	*0.069*	−0.042	0.001	0.003	0.002			

[a] V−W, V−V nearest to W, and other V−V distances are rendered in bold, italic, and plain text, respectively. See Figure 5a for locations of the chains.

Table 7. Differences in the Intercationic Distances (Å) along the Central (W-Containing) and Four Closest Parallel Chains in the W-Doped VO_2 Monoclinic Phase and Two Chains within the Pure VO_2 Monoclinic Phase Relative to the V−V Distance Found in the Pure Tetragonal Phase (2.860 Å)[a]

pure	−0.201	0.071	−0.201	0.071	−0.201	0.071	−0.201	0.071	−0.201			
down	−0.201	0.064	−0.203	0.069	*−0.193*	0.076	−0.201	0.068	−0.201			
front	−0.201	0.066	−0.202	0.071	*−0.195*	0.074	−0.201	0.068	−0.201			
central	−0.200	0.091	−0.183	−0.184	**0.061**	**0.061**	−0.207	0.045	−0.202	0.066		
up	0.071	−0.201	0.056	−0.202	*0.092*	−0.201	0.069	−0.201	0.068			
back	0.071	−0.201	0.053	−0.203	*0.104*	−0.203	0.064	−0.201	0.067			
pure	0.071	−0.201	0.071	−0.201	0.071	−0.201	0.071	−0.201	0.071			

[a] V−W, V−V nearest to W, and other V−V distances are rendered in bold, italic, and plain text, respectively. See Figure 5b for locations of the chains.

solution. This result is somewhat in excess of the experimentally observed reduction of 26 K per 1%,[3] although considering the approximations in our model, the agreement was acceptable.

Summary

We have developed interatomic potential parameters for modeling the phases of VO_2 and $V_{1-\delta}W_\delta O_2$. The low-temperature phase of VO_2 can be visualized as the Peierls-distorted high-temperature phase. In fact, there are two equivalent low-temperature structures. Following one of the lowest-energy transition pathways leading from the pure tetragonal (high-temperature) phase, one of the two cation chains (edge-sharing VO_6 octahedra) undergoes a Peierls distortion until the saddle point is reached, after which both chains distort. Upon doping with W, we calculated that a 1% dopant solution would reduce the phase transition temperature by 48.4 K. The W ion induces a localized Peierls distortion in the high-temperature phase, whereas in the low-temperature phase, a symmetrical local environment about the W ion exists and a second structural defect along the cation chain is created. Currently we are investigating higher concentrations of dopants and their inactions; this work also implements the AOM model in order to include Jahn–Teller distortions in our calculations.

Acknowledgment. We thank The Royal Society and the NRF collaborative project on materials modeling for support and funding and our colleague Spencer Braithwaite for his valuable contribution to our initial investigations. S.M.W. and C.R.A.C. also acknowledge funding from EPSRC (Grant EP/D504872) and the use of Materials Studio visualization software from Accelrys.

CM701861Z